Structural and electronic origin of the magnetic structures in hexagonal $LuFeO_3$

Hongwei Wang,[1,2] Igor V. Solovyev,[3] Wenbin Wang,[4] Xiao Wang,[5] Philip J. Ryan,[6] David J. Keavney,[6] Jong-Woo Kim,[6] Thomas Z. Ward,[7] Leyi Zhu,[8] Jian Shen,[4] X. M. Cheng,[5] Lixin He,[2] Xiaoshan Xu,[5,7,9,*] and Xifan Wu[2,*]

[1]*Department of Physics, Temple University, Philadelphia, Pennsylvania 19122, USA*
[2]*Key Laboratory of Quantum Information, University of Science and Technology of China, Hefei, Anhui 230026, People's Republic of China*
[3]*Computational Materials Science Unit, National Institute for Materials Science, 1-2-1 Sengen, Tsukuba 305-0047, Japan*
[4]*Department of Physics, Fudan University, Shanghai 200433, People's Republic of China*
[5]*Department of Physics, Bryn Mawr College, Bryn Mawr, Pennsylvania 19010, USA*
[6]*Advanced Photon Source, Argonne National Laboratory, Argonne, Illinois 60439, USA*
[7]*Materials Science and Technology Division, Oak Ridge National Laboratory, Oak Ridge, Tennessee 37831, USA*
[8]*Materials Science Division, Argonne National Laboratory, Argonne, Illinois 60439, USA*
[9]*Department of Physics and Astronomy, University of Nebraska, Lincoln, Nebraska 68588, USA*

(Received 16 February 2014; revised manuscript received 7 July 2014; published 29 July 2014)

Using combined theoretical and experimental approaches, we studied the structural and electronic origin of the magnetic structure in hexagonal $LuFeO_3$. Besides showing the strong exchange coupling that is consistent with the high magnetic ordering temperature, the previously observed spin reorientation transition is explained by the theoretically calculated magnetic phase diagram. The structural origin of this spin reorientation that is responsible for the appearance of spontaneous magnetization, is identified by theory and verified by x-ray diffraction and absorption experiments.

DOI: 10.1103/PhysRevB.90.014436 PACS number(s): 75.85.+t, 77.55.Nv

I. INTRODUCTION

While the ferroelectricity in materials is naturally connected to structural distortions that break the spatial inversion symmetry [1,2], the relation between spontaneous magnetization and structure is not obvious because no spatial symmetry is broken by ferromagnetism (FM). Nevertheless, magnetic orderings in a material are tied to the structure, and the ties are particularly important in multiferroic materials [3] in which structural distortions may mediate couplings between ferroelectricity and ferromagnetism or even generate ferroelectric ferromagnets, which are extremely rare [4].

The recently discovered room temperature multiferroic, i.e., hexagonal $LuFeO_3$ (hLFO) [5], provides a rare case of multiferroic material in which spontaneous electric and magnetic polarizations coexist. On one hand, ferroelectricity appears below $T_C = 1050$ K resulting from a $P6_3/mmc \rightarrow P6_3cm$ structure distortion, which can be decomposed in terms of three phonon modes [Fig. 1(a)] [5,6]. On the other hand, spin frustration in hLFO presents rich magnetic phases [7]. Intriguingly, below the Neél temperature $T_N = 440$ K, magnetic order in hLFO transits again from B_2 to A_2 [Fig. 1(b)] at $T_R = 130$ K [5] by a spin reorientation (SR), resulting in a weak ferromagnetism due to the Dzyaloshinskii-Moriya and single-ion anisotropy mechanism [8–12]. Similar to hexagonal $YMnO_3$, the K_3 phonon is believed to be the driving force that induces the instability of Γ_2^- that is responsible for the ferroelectricity [13–15]. However, the origin of the SR is still elusive. Since the SR is the direct cause of spontaneous magnetization, elucidating the origin may provide a way to effectively tune T_R, or even a novel route for realizing a coexistence of spontaneous electric and magnetic polarizations above room temperature [16–18].

Previous studies in hexagonal manganites (h-RMO, isomorphic to hLFO) indicate rich magnetic phases due to the SR that is strongly coupled to the crystal structure [3,19,20]. However, the multiple degrees of freedom involved (spin and orbital degrees of freedom of the electrons and the lattice) complicate the problem in h-RMO [21]. The complexity may be reduced in h-LFO, in which Fe^{3+} can be considered a spin-only ion with nearly spherical $3d^5$ electronic configuration. Therefore, a better understanding of the SR in hLFO is possible, particularly in terms of the phonon modes [Fig. 1(b)]; it may also be an important step in understanding the more complex SR in h-RMO [21], in which the single-ion anisotropy is expected to play a more important role.

To address the above issues, we perform combined theoretical and experimental studies of the exchange interactions and their couplings to the structural instabilities in hLFO. We apply an extended Kugel-Khomskii (KK) model for superexchange (SE) interactions [22] based on localized Wannier functions (LWFs) [23,24]. While the antiferromagnetic (AFM) exchange coupling is dominated by the intralayer superexchange, the model clearly shows that the singly occupied d_{z^2} orbital in hLFO greatly increases the exchange coupling compared with the empty d_{z^2} in $LuMnO_3$ (LMO). The interlayer exchange, although much weaker in magnitude, is key to the SR. Our first-principles calculations show that SR is strongly coupled to the K_1 phonon mode and only weakly dependent on K_3 mode. Our theory indicates that the atomic displacements of K_1 mode is responsible for the SR. This scenario is then confirmed by our x-ray diffraction and x-ray absorption experiments.

II. COMPUTATIONAL METHODS AND EXPERIMENTAL TECHNIQUES

Our extended KK model [22,25] is built on the basis of LWFs generated from density functional theory (DFT) calculations. The screened Coulomb interactions between LWFs are computed in the constrained random-phase approximation

*Authors to whom correspondence should be addressed: xifanwu@temple.edu and xiaoshan.xu@unl.edu

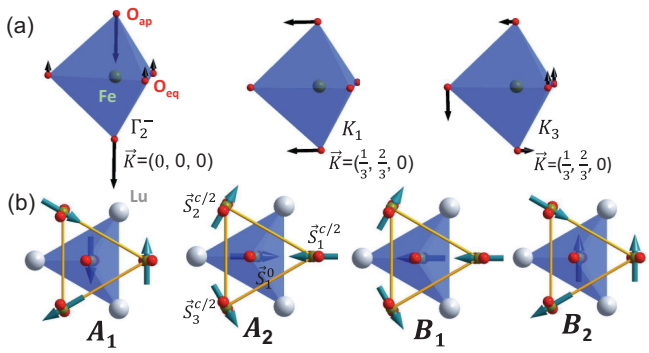

FIG. 1. (Color online) (a) Displacement patterns of the FeO_5 local environment (trigonal bipyramid) in the three phonon modes that freeze in the $P6_3/mmc \rightarrow P6_3cm$ structural transition in hexagonal ferrites (h-$RFeO_3$). The arrows indicate the relative displacement of the atoms. $\vec{K}$ is the wave vector of the modes in the reciprocal space of the $P6_3/mmc$ structure. (b) Four independent spin structures (A_1, A_2, B_1, and B_2) of the 120-degree magnetic orders viewed along the c axis. The arrows indicate the spins ($\vec{S}_i^{Z_{Fe}}$) on the Fe sites. The Fe sites shown in the polyhedra are in the $Z_{Fe} = 0$ layer while all the other Fe sites are in the $Z_{Fe} = c/2$ layers. In the B (A) phase, $\vec{S}_1^0$ is parallel (antiparallel) to $\vec{S}_1^{c/2}$.

[25–27]. The calculations of spin phonon coupling is performed within DFT+U scheme [25,28]. We have adopted the four-state method [29] in computing the exchange coupling strengths. hLFO films (50 nm thick) were grown on Al_2O_3 (0001) substrates with and without a (30 nm) Pt buffer layer using pulsed laser deposition. The x-ray diffraction (XRD) and x-ray absorption spectroscopy (XAS) measurements were carried out in the 6-ID-B beam line on the h-$LuFeO_3/Al_2O_3$ film and in the 4-ID-C beam line on the h-$LuFeO_3$/Pt/Al_2O_3 film at the Advanced Photon Source at various temperature.

III. RESULTS AND DISCUSSION

In hexagonal ferrites, the exchange interaction between the Fe sites can be written as

$$H_{ex} = H_{ex}^{a-b} + H_{ex}^{c} \tag{1}$$

where H_{ex}^{a-b} is the intralayer exchange interaction and H_{ex}^{c} is the interlayer exchange interaction considering only the nearest neighbors.

As shown in Fig. 2, the intralayer SE interaction $H_{ex}^{a-b} = \sum_{i,j,Z_{Fe}} \mathcal{J}_{i,j}^{a-b} \vec{S}_i^{Z_{Fe}} \cdot \vec{S}_j^{Z_{Fe}}$ between two nearest neighbor (NN) Fe atoms at site i and j are mediated by corner sharing oxygen atoms. In order to elucidate the electronic structural origin, we employ the extended KK model, and the SE coupling can be expressed as

$$\mathcal{J}_{i,j}^{a-b} = \sum_{\alpha,\alpha'} J_{\alpha,\alpha'}^{\mathrm{AFM}} + \sum_{\alpha,\beta} J_{\alpha,\beta}^{\mathrm{FM}}. \tag{2}$$

The first term in Eq. (2) describes the AFM-type coupling resulting from virtual hopping processes between two half-filled d bands; while the second term depicts the competing FM-type coupling from hoppings from a half-filled d orbital (α) to empty ones (β) [25]. The computed individual exchange interaction as well as the overall SE coupling J_{MOD}^{a-b} for both

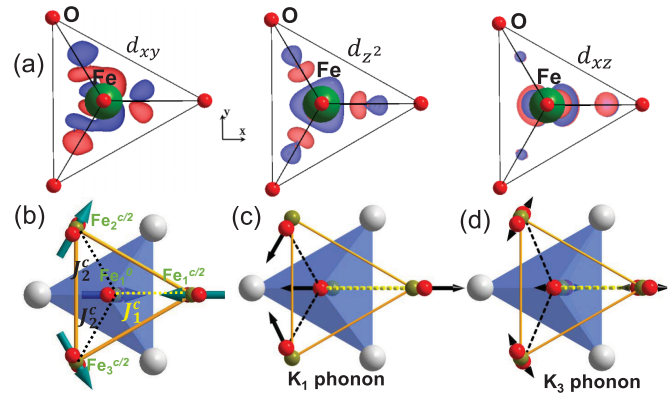

FIG. 2. (Color online) (a) Representative d_{xy}, d_{z^2}, and d_{xz}-like LWFs viewed from [001] direction. (b) Illustrations of two independent SSE paths J_1^c and J_2^c between Fe_0 at $z/c = 0$ and three neighboring iron ions Fe_1, Fe_2, and Fe_3 at $z/c = 1/2$ (c) Atomic displacements of the K_1 phonon mode. (d) Atomic displacements of the K_3 phonon mode, viewed from [001] direction.

hLFO and hLMO are presented in Table I. The total exchange couplings J_{DFT}^{a-b} from the direct fit of the total DFT energies are also shown.

According to the local environment (Fig. 1), the 3d orbitals in Fe and Mn are split into $e''(xz,yz)$, $e'(x^2-y^2,xy)$, and $a_1'(z^2)$ levels by the crystal field, with increasing energy respectively [30,31]. It can be seen that the largest SE interactions are contributed by the diagonal hopping processes involving d orbitals of e' symmetry. This is consistent with the physical expectation that SE is of intralayer nature while d_{xy} and $d_{x^2-y^2}$ are the only d orbitals lying mostly inside the ab plane. Centered on the magnetic ions, these d-like LWFs are also connected with the first neighboring magnetic atoms through hybridization with the shared oxygen atoms on the bipyramids. As a result, a strong oxygen p character is found on the lobe of the LWFs, pointing to each of the three neighboring oxygen atoms. Considering such d-like LWFs on the hexagonal lattices, a large AFM hopping integral is thus expected along the path of Fe(Mn)-O-Fe(Mn) [32]. Based on the same orbital symmetry argument, it can be easily seen that the diagonal hopping is relatively smaller for $a_1'(z^2)$ character and almost zero for e'' character. This is because d_{z^2} and d_{xz}

TABLE I. Individual and total intralayer exchange interaction (meV) in both hLFO and hLMO [25].

$J_{\alpha,\alpha'(\beta)}$		d_{xy}	$d_{x^2-y^2}$	d_{z^2}	d_{xz}	d_{yz}	J_{MOD}^{ab}	J_{DFT}^{ab}
hLFO	d_{xy}	9.49	3.65	3.20	1.14	0.47	45.2	49.7
	$d_{x^2-y^2}$	0.68	9.90	0.88	1.04	0.05		
	d_{z^2}	1.25	5.05	3.58	1.25	0.27		
	d_{xz}	0.56	0.09	0.14	0.01	0.06		
	d_{yz}	0.32	1.00	0.65	0.37	0.06		
hLMO	d_{xy}	10.15	5.81	−0.64	1.17	0.78	29.3	30.7
	$d_{x^2-y^2}$	1.28	10.9	−2.71	0.85	0.12		
	d_{z^2}							
	d_{xz}	0.41	0.17	−0.43	0.01	0.08		
	d_{yz}	0.39	0.85	−0.19	0.31	0.04		

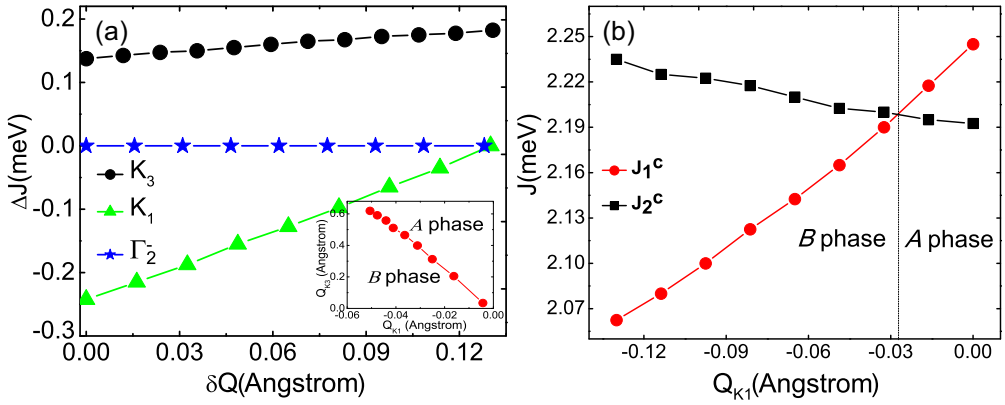

FIG. 3. (Color online) (a) $\Delta J(\delta Q) = J(Q) - J(Q_0)$ for each individual K_1, K_3, and Γ_2^- phonon mode, where $\delta Q = Q - Q_0$ and Q_0 is the value at 300 K, while the other two phonon displacements are kept as zero. Inset: theoretical phase diagram as functions of mode amplitudes of K_1 and K_3. (b) J_1^c and J_2^c as functions of Q_{K_1}, while Q_{K_3} and $Q_{\Gamma_2^-}$ are fixed at the experimental values [25].

(d_{yz}) require that the main orbital lobe be located along z or within the xz (yz) plane, which makes the hopping integrals much smaller.

Strikingly, the SE interactions also show fundamental differences between the two materials. In hLFO (Fe^{3+}:$3d^5 4s^0$), the d_{z^2} orbital of a_1' symmetry is singly occupied, and SE interactions can only be of AFM types. However, d_{z^2} is empty in hLMO (Mn^{3+}:$3d^4 4s^0$), SE interactions are thus composed of competing AFM and FM types, and the coupling strength is further reduced by the forbidden hopping involving the empty d_{z^2}. Thus, a significantly larger AFM coupling energy is observed in hLFO. This is consistent with the higher Neél temperature in hLFO observed in experiment in addition to the larger spin on the Fe site.

Having established the electronic origin of the large intralayer exchange coupling, we now focus on the interlayer exchange coupling $H_{ex}^c = \sum_{i,j,Z_{Fe}} \mathcal{J}_{i,j}^c \vec{S}_i^{Z_{Fe}} \cdot \vec{S}_j^{Z_{Fe}+\frac{c}{2}}$ in hLFO. This is the key to understanding the mechanism of SR and weak FM moment below T_R [5]. In contrast to the SE nature of intralayer exchange, the interlayer Fe ions are coupled by the super-super-exchange (SSE) interaction [33], in which one Fe atom at $Z_{Fe} = 0$ is in exchange interaction with three first neighbor Fe atoms at $Z_{Fe} = c/2$ mediated by two apical oxygen atoms (O_{ap}). Due to the $P6_3cm$ structure in Fig. 3 (b), the three SSE paths can be further simplified by two independent SSE coupling strengths: J_1^c through Fe_1^0-O- $\cdots$ -O-$Fe_1^{\frac{c}{2}}$ and J_2^c through Fe_1^0-O- $\cdots$ -O-$Fe_2^{\frac{c}{2}}$. As a result, the H_{ex}^c spin Hamiltonian in Eq. (1) can be rewritten as $H_{ex}^c = \sum_{i,Z_{Fe}} (J_1{}^c - J_2{}^c) \vec{S}_i^{Z_{Fe}} \cdot \vec{S}_i^{Z_{Fe}+\frac{c}{2}}$. Obviously, the sign of $\Delta J = J_1^c - J_2^c$ determines the preferred alignment between $\vec{S}_i^{Z_{Fe}}$ and $\vec{S}_i^{Z_{Fe}+\frac{c}{2}}$: parallel ($B$ phase) if $\Delta J < 0$; antiparallel (A phase) if $\Delta J > 0$; no alignment if $\Delta J = 0$, which is the case for $P6_3/mmc$ structure.

Since the nonzero ΔJ comes from the structural distortion ($P6_3/mmc \rightarrow P6_3cm$), the low temperature spin reorientation must have a structural origin. Here we investigate the dependence of ΔJ on the three phonon modes K_1, K_3, and Γ_2^- that are responsible for the structural distortion [25]. We use DFT to calculate the ΔJ as functions of phonon mode displacements (Q_p, where $p = K_1, K_3$, and Γ_2^-) and the results are shown in Fig. 3(a). It can be seen that ΔJ depends on the displacement of each phonon mode rather differently.

Clearly, the K_1 phonon mode has the largest effect on SR. This can be identified by the steepest slope of ΔJ when K_1 is increased perturbatively, yielding a linear coefficient $\frac{\delta \Delta J}{\delta Q_{K_1}} \sim 1.9$ meV/Å. This suggests a strong tendency of K_1 in driving hLFO from B phase ($\Delta J < 0$) into A phase ($\Delta J > 0$). Indeed this is also consistent with the physical expectation of atomic displacements under the K_1 mode. The K_1 phonon is a Brillouin zone (BZ) boundary mode and is of pure in-plane nature. The atomic displacements of the K_1 phonon mostly involve the O_{ap} of FeO_5 (Fig. 1). As shown in Fig. 2(c), the effects of the K_1 are as follows: O_{ap} of Fe_1^0 moves away from that of $Fe_1^{\frac{c}{2}}$, causing J_1^c to decrease; and O_{ap} of Fe_1^0 moves closer to that of $Fe_2^{\frac{c}{2}}$ and $Fe_3^{\frac{c}{2}}$, causing J_2^c to increase. As a result, K_1 is strongly coupled to the ΔJ.

The K_3 phonon mode can be described by the rotation of FeO_5 [Fig. 1(a)] also located at BZ boundary. The atomic displacements of the K_3 mode include all the O_{ap} of the FeO_5. However, due to its rotational nature, the atomic displacement of the O_{ap} alternate their directions along c as shown in Fig. 2(d). As a result, the overall lengths of J_1^c and J_2^c paths are barely changed except that the Fe atom is slightly moved away from its equilibrium positions in $P6_3/mmc$ symmetry. Compared with the direct tunability of ΔJ by the K_1 mode, the K_3 phonon is expected to be a second-order effect in SR. Indeed, our DFT calculation predicts a much weaker variation of ΔJ with increased K_3 phonon mode amplitude, in which the linear coefficient $\frac{\delta \Delta J}{\delta Q_{K_3}} \sim 0.3$ meV/Å is about one order of magnitude smaller than that of K_1. Similar to that of K_1 mode, the slope is also positive, favoring the SR from B to A phase.

Finally, we focus on the coupling between Γ_2^- and ΔJ. Γ_2^- is the ferroelectric phonon mode at zone center. The atomic displacements of this mode involve all the Lu, O, and Fe atoms moving along c. However, the displacements of the two O_{ap} of one bipyramid are exactly the same. As a result, the SSE paths in J_1^c and J_2^c are changed uniformly. Not surprisingly, our theory predicts a zero dependence of ΔJ on Γ_2^- mode amplitude. It indicates that this ferroelectric distortion alone does not play any role in SR.

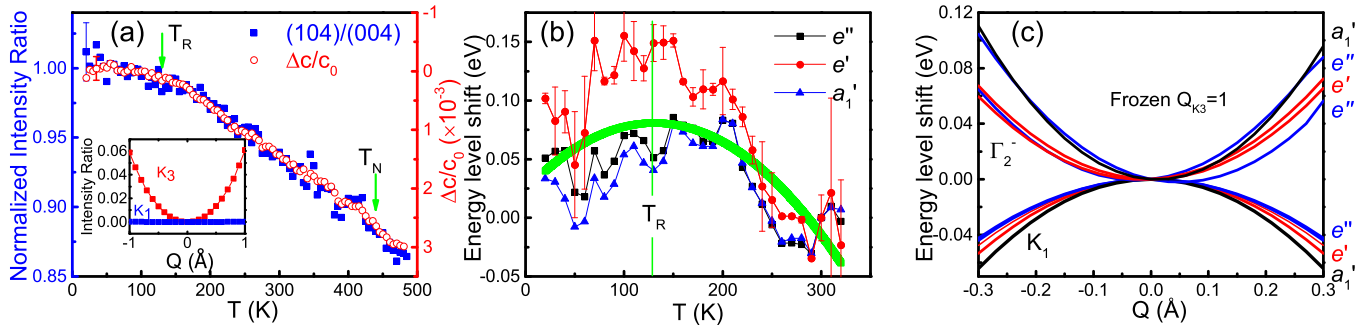

FIG. 4. (Color online) Structural changes indicated by the XRD and XAS. (a) The XRD intensity ratio between the (104) and (004) peaks (normalized to the 30 K value) and the change of lattice constant c (with respect to the 30 K value) as functions of the temperature (the representative error bars are shown). Inset: the simulated intensity ratio between the (104) and (004) peaks as functions of phonon displacements. (b) The change of Fe-3d crystal field levels (relative to the 300 K values) as functions of the temperature (the error bars for e' levels are shown as examples); the bold line is a guide to the eye to highlight the common peak-like feature. (c) Simulated change of Fe-3d levels as functions of phonon displacements [25].

The significantly different coupling strengths of ΔJ with the phonon modes suggests the primary role of the K_1 phonon mode in SR of hLFO. Indeed, when the K_1 mode is frozen into the experimental structural coordinates at $T = 300$ K perturbatively, J_1^c and J_2^c rapidly increase and decrease respectively, and SR occurs at the crossing point as shown in Fig. 3(b) separating the B from A phases. Below, we show that Q_{K_3} saturates close to T_R, while Q_{K_1} changes significantly from 300 to 20 K using XRD and XAS measurements.

As shown in Fig. 4(a), the temperature dependence of the normalized intensity ratio between (104) and (004) peaks appears to saturate when temperature is lowered to T_R. We attribute the saturation to the slow variation of the K_3 phonon at low temperature, because K_3 is expected to have a dominant effect here, according to the simulated intensity ratio [Fig. 4(a) inset] [34], while the zone center mode Γ_2 is expected to have no effect. The saturation of the K_3 mode can be further confirmed by the temperature dependence of the lattice constant c which follows closely that of the intensity ratio, as shown in Fig. 4(a). The displacement of the K_3 mode includes a rotation of the FeO_5 trigonal bipyramid, which changes the shape of the unit cell by enlarging a and reducing c [7]; the change of c (Δc) is proportional to ΔQ_{K_3} for small change of Q_{K_3}. The matching temperature dependence in Fig. 4(a) suggests that the change of c is indeed caused by the K_3 mode which saturates at low temperature.

XAS measurements suggest that the K_1 mode undergoes a gradual change at low temperature. Previously, we assigned the Fe-3d crystal levels using the XAS at room temperature [25,30]. As shown in Fig. 4(b), the temperature dependences of the energy levels all show broad peak-like features with the maxima close to T_R. The crystal field levels of Fe-3d are expected to be sensitive to the shape of FeO_5. As shown in Fig. 1(a), the K_3 mode causes a rotation of the FeO_5 while the K_1 or Γ_2^- modes cause distortions of the FeO_5, so the energy-level shifts observed in Fig. 4(c) are most likely generated by the change of Q_{K_1} or $Q_{\Gamma_2^-}$. Figure 4(c) shows a simulation [25] of the energy-level change of the crystal field levels as functions of Q_{K_1} or $Q_{\Gamma_2^-}$ with respect to the value when all the mode displacements are zero. According to the simulation, the K_1 mode generates a maximum at $Q_{K_1} = 0$ while $Q_{\Gamma_2^-}$ generates a minimum at $Q_{\Gamma_2^-} = 0$; this is because the K_1 mode moves both O_{ap} atoms away from the Fe sites and makes the FeO_5 larger while the Γ_2^- mode pushes one O_{ap} atom close to the Fe site. Comparing the simulation and the observation, we infer that the K_1 mode changes gradually when the temperature is lowered, in order to generate the maximum [25]; this is consistent with the theoretical prediction in which Q_{K_1} changes when the temperature is lowered and causes the transition from antiferromagnetism in the B_2 phase to weak ferromagnetism in the A_2 phase.

IV. CONCLUSION

The roles of all three structural distortions are elucidated in hLFO: the instability of the K_3 mode is the driving force of the $P6_3/mmc \rightarrow P6_3cm$ structural transition; the improper ferroelectricity of the Γ_2^- mode is induced by the frozen K_3 mode [13,15]; and the competing effect between K_1 and K_3 modes determines the magnetic ordering and drives the magnetic phase transition. If the K_1 mode can be tuned by interface engineering [35–37], the T_R can be increased, achieving the spontaneous electric and magnetic polarizations and their couplings at room temperature.

ACKNOWLEDGMENTS

This work is supported by Air Force Office of Scientific Research under Grant No. FA9550-13-1-0124 (X.W.). Computational support is provided by the National Energy Research Scientific Computing Center and by the National Science Foundation through XSEDE resources provided by the XSEDE Science Gateways program (Award No. TG-DMR120045). Research was supported by the US Department of Energy, Basic Energy Sciences, Materials Sciences and Engineering Division (T.Z.W. and X.S.X.). We also acknowledge partial funding support from the National Basic Research Program of China (973 Program) under Grant No. 2011CB921801 (J.S.), from the National Natural Science Funds of China, Grant No. 11374275 (L.H.) and from the US DOE Office of

Basic Energy Sciences, Grant No. DE-SC0002136 (W.B.W.). Use of the Advanced Photon Source was supported by the US Department of Energy, Office of Science, Office of Basic Energy Sciences, under Contract No. DE-AC02-06CH11357. X.M.C. acknowledges support from the National Science Foundation under Grant No. 1053854. X.W. is grateful for useful discussions with Andrei Malashevich, Craig Fennie, Weida Wu, and David Vanderbilt.

[1] M. Stengel, N. A. Spaldin, and D. Vanderbilt, Nat. Phys. **5**, 304 (2009).
[2] H. Fu and R. E. Cohen, Nature (London) **403**, 281 (2000).
[3] S. Lee, A. Pirogov, M. Kang, K.-H. Jang, M. Yonemura, T. Kamiyama, S.-W. Cheong, F. Gozzo, N. Shin, H. Kimura, Y. Noda, and J.-G. Park, Nature (London) **451**, 805 (2008).
[4] J. H. Lee *et al.*, Nature (London) **466**, 954 (2010).
[5] W. Wang, J. Zhao, W. Wang, Z. Gai, N. Balke, M. Chi, H. N. Lee, W. Tian, L. Zhu, X. Cheng, D. J. Keavney, J. Yi, T. Z. Ward, P. C. Snijders, H. M. Christen, W. Wu, J. Shen, and X. Xu, Phys. Rev. Lett. **110**, 237601 (2013).
[6] E. Magome, C. Moriyoshi1, Y. Kuroiwa1, A. Masuno and H. Inoue, Jpn. J. Appl. Phys. **49**, 09ME06 (2010).
[7] A. Muñoz, J. A. Alonso, M. J. Martínez-Lope, M. T. Casáis, J. L. Martínez, and M. T. Fernández-Díaz, Phys. Rev. B **62**, 9498 (2000).
[8] A. R. Akbashev, A. S. Semisalova, N. S. Perov, and A. R. Kaul, Appl. Phys. Lett. **99**, 122502 (2011).
[9] I. Dzyaloshinsky, J. Phys. Chem. Solids **4**, 241 (1958).
[10] T. Moriya, Phys. Rev. **120**, 91 (1960).
[11] A. Malashevich and D. Vanderbilt, Phys. Rev. Lett. **101**, 037210 (2008).
[12] J. Hong, A. Stroppa, J. Íñiguez, S. Picozzi, and D. Vanderbilt, Phys. Rev. B **85**, 054417 (2012).
[13] H. Das, A. L. Wysocki, Y. Geng, W. Wu, and Craig J. Fennie, Nat. Commun. **5**, 2998 (2014).
[14] Y. Geng, H. Das, A. L. Wysocki, X. Wang, S.-W. Cheong, M. Mostovoy, C. J. Fennie, and W. Wu, Nat. Mater. **13**, 163 (2014).
[15] C. J. Fennie and K. M. Rabe, Phys. Rev. B **72**, 100103(R) (2005).
[16] N. A. Spaldin, S.-W. Cheong, and R. Ramesh, Phys. Today **63**, 38 (2010).
[17] J. Wang *et al.*, Science **299**, 1719 (2003).
[18] J. B. Neaton, C. Ederer, U. V. Waghmare, N. A. Spaldin, and K. M. Rabe, Phys. Rev. B **71**, 014113 (2005).
[19] T. Lancaster, S. J. Blundell, D. Andreica, M. Janoschek, B. Roessli, S. N. Gvasaliya, K. Conder, E. Pomjakushina, M. L. Brooks, P. J. Baker, D. Prabhakaran, W. Hayes, and F. L. Pratt, Phys. Rev. Lett. **98**, 197203 (2007).
[20] X. Fabrèges, S. Petit, I. Mirebeau, S. Pailhès, L. Pinsard, A. Forget, M. T. Fernandez-Diaz, and F. Porcher, Phys. Rev. Lett. **103**, 067204 (2009).
[21] P. J. Brown and T. Chatterji, J. Phys. Condens. Matter **18**, 10085 (2006).
[22] K. I. Kugel and D. I. Khomskii, Sov. Phys. Usp. **25**, 231 (1982).
[23] N. Marzari, A. A. Mostofi, J. R. Yates, I. Souza, D. Vanderbilt *et al.*, Rev. Mod. Phys. **84**, 1419 (2012).
[24] P. H.-L. Sit, Roberto Car, Morrel H. Cohen, and A. Selloni, Inorg. Chem. **50**, 10259 (2011).
[25] See Supplemental Material at http://link.aps.org/supplemental/10.1103/PhysRevB.90.014436 for more detailed information on the theoretical model and calculation, phonon mode decomposition, analysis of the x-ray absorption spectra, and simulation of crystal field levels.
[26] I. V. Solovyev, M. V. Valentyuk, and V. V. Mazurenko, Phys. Rev. B **86**, 054407 (2012).
[27] I. V. Solovyev, J. Phys: Condens. Matter **20**, 293201 (2008).
[28] G. Kresse and J. Furthmüller, Phys. Rev. B **54**, 11169 (1996).
[29] H. J. Xiang, E. J. Kan, S.-H. Wei, M.-H. Whangbo, and X. G. Gong, Phys. Rev. B **84**, 224429 (2011).
[30] W. Wang, H. Wang, X. Xu, L. Zhu, L. He, E. Wills, X. Cheng, D. J. Keavney, J. Shen, X. Wu, and X. Xu, Appl. Phys. Lett. **101**, 241907 (2012).
[31] D.-Y. Cho, J.-Y. Kim, B.-G. Park, K.-J. Rho, J.-H. Park, H.-J. Noh, B. J. Kim, S.-J. Oh, H.-M. Park, J.-S. Ahn, H. Ishibashi, S.-W. Cheong, J. H. Lee, P. Murugavel, T. W. Noh, A. Tanaka, and T. Jo, Phys. Rev. Lett. **98**, 217601 (2007).
[32] P. W. Anderson, Phys. Rev. **79**, 350 (1950).
[33] M.-H. Whangbo, H.-J. Koo, and D. Dai, J. Solid. State. Chem. **176**, 417 (2003).
[34] B. D. Cullity, *Elements of X-Ray Diffraction* (Addison-Wesley, Reading, MA, 1956).
[35] J. H. Lee and K. M. Rabe, Phys. Rev. Lett. **104**, 207204 (2010).
[36] O. Diéguez, K.M. Rabe, and D. Vanderbilt, Phys. Rev. B **72**, 144101 (2005).
[37] J. Junquera and P. Ghosez, Nature (London) **422**, 506 (2003).

Supporting Online Material

Structural and electronic origin of the magnetic structures in hexagonal $LuFeO_3$

Hongwei Wang[1,2], Igor V. Solovyev[3], Wenbin Wang[4], Xiao Wang[5], Phillip Ryan[6], David J. Keavney[6], Jong-Woo Kim[6], Thomas Z. Ward[7], Leyi Zhu[8], X. M. Cheng[5], Jian Shen[4], Lixin He[2], Xiaoshan Xu[5,7,9,*], and Xifan Wu[1,*]

[1]*Department of Physics, Temple University, Philadelphia, Pennsylvania 19122, USA*

[2]*Key Laboratory of Quantum Information, University of Science and Technology of China, Hefei, Anhui, 230026, People's Republic of China*

[3]*Computational Materials Science Unit, National Institute for Materials Science, 1-2-1 Sengen, Tsukuba 305-0047, Japan*

[4]*Department of Physics, Fudan University, Shanghai 200433, China*

[5]*Department of Physics, Bryn Mawr College, Bryn Mawr, PA 19010, USA*

[6]*Advanced Photon Source, Argonne National Laboratory, Argonne, IL 60439, USA*

[7]*Materials Science and Technology Division, Oak Ridge National Laboratory, Oak Ridge, TN 37831, USA*

[8]*Materials Science Division, Argonne National Laboratory, Argonne, IL 60439, USA and*

[9]*Department of Physics, University of Nebraska-Lincoln, NE 68588-0299, USA*

I. DENSITY FUNCTIONAL THEORY (DFT) FITTED MODEL HAMILTONIAN

The model Hamiltonian,

$$\hat{\mathcal{H}} = \sum_{ij}\sum_{\alpha\beta} t_{ij}^{\alpha\beta}\hat{c}_{i\alpha}^{\dagger}\hat{c}_{j\beta} + \frac{1}{2}\sum_{i}\sum_{\alpha\beta\gamma\delta} U_{\alpha\beta\gamma\delta}^{i}\hat{c}_{i\alpha}^{\dagger}\hat{c}_{i\gamma}^{\dagger}\hat{c}_{i\beta}\hat{c}_{i\delta}, \tag{1}$$

is formulated in the basis of Wannier orbitals $\{\phi_{i\alpha}\}$, which are constructed for the magnetically active bands near the Fermi level. Here, each Greek symbol (α, β, γ, or δ) stands for the combination of spin (σ= + or −) and orbital (a, b, c, or d) indices: for instance, $\alpha \equiv (\sigma_\alpha, a)$, etc. The orbital indices for the $3d$ orbitals are xy, yz, $3z^2-r^2$, zx, and x^2-y^2.

The model is constructed for the magnetically active $3d$ bands of $LuFeO_3$ and $LuMnO_3$, located near the Fermi level, and starting from the electronic band structure obtained in the local-density approximation (LDA). This calculations have been performed using linear muffin-tin orbital (LMTO) method.[1] The first step is the construction of localized Wannier basis for these low-energy bands. Each basis orbital $\phi_{i\alpha}(\mathbf{r})$ is labeled by the combined index α and centered around some lattice point i. In our case, the Wannier function have been generated using the projector-operator method (Refs. 2–4) and pseudo-atomic $3d$ basis orbitals of the LMTO method as the trial wave functions. As the LMTO basis functions are already well localized, typically such procedure allows us to generate well localized Wannier functions. This property will be discussed below. Then, the one-electron part of the model is identified with the matrix elements of LDA Hamiltonian ($\mathcal{H}_{\rm LDA}$) in the Wannier basis: $t_{ij}^{\alpha\beta} = \langle\phi_{i\alpha}(\mathbf{r})|\mathcal{H}_{\rm LDA}|\phi_{j\beta}(\mathbf{r})\rangle$. Since the Wannier basis is complete in the low-energy part of the spectrum, the construction is exact in a sense that the band structure, obtained from $t_{ij}^{\alpha\beta}$, coincides with the one of LDA. Without relativistic spin-orbit interaction, matrix elements $t_{ij}^{\alpha\beta}$ do not depend on the spin indices: $t_{ij}^{\alpha\beta} \equiv t_{ij}^{ab}\delta_{\sigma_\alpha,\sigma_\beta}$. Then, the site-diagonal elements $\equiv t_{ii}^{ab}$ describe effects of the crystal-field splitting and off-diagonal elements t_{ij}^{ab} ($i \neq j$) stand for the transfer integrals (or hoppings).

Matrix elements of screened Coulomb interactions at some atomic site i can be also calculated in the Wannier basis as

$$U_{\alpha\beta\gamma\delta}^{i} = \int d\mathbf{r}\int d\mathbf{r}'\phi_{i\alpha}^{*}(\mathbf{r})\phi_{i\beta}(\mathbf{r})v_{\rm scr}(\mathbf{r},\mathbf{r}')\phi_{i\gamma}^{*}(\mathbf{r}')\phi_{i\delta}(\mathbf{r}'). \tag{2}$$

The screened Coulomb interaction $v_{\rm scr}(\mathbf{r},\mathbf{r}')$ can be calculated by employing the constrained random-phase approximation (RPA) technique.[5] Then, $v_{\rm scr}(\mathbf{r},\mathbf{r}')$ does not depend on spin

variables and, therefore, $U^i_{\alpha\beta\gamma\delta}$ has the following spin structure: $U^i_{\alpha\beta\gamma\delta} = U^i_{abcd}\,\delta_{\sigma_\alpha\sigma_\beta}\delta_{\sigma_\gamma\sigma_\delta}$. Since the constrained RPA technique is very time consuming (and still not affordable for hexagonal $LuFeO_3$ and $LuMnO_3$, containing up to 30 atoms in the unit cell), we apply additional approximations, which were discussed in Ref. 4. Namely, first we evaluate the screened Coulomb and exchange interactions between atomic $3d$ orbitals, using fast and more suitable for these purposes constrained LDA technique. After that, we consider additional channel of screening caused by the $3d \to 3d$ transitions involving these atomic orbitals in the framework of constrained RPA technique. The so obtained parameters of Coulomb interactions are well consistent with results of full-scale constrained RPA calculations.[6]

In order to illustrate how well our Wannier functions are localized in space we plot in Fig. 1 averaged transfer integrals, $\bar{t}_{ij} = \sqrt{\sum_{ab}(t^{ab}_{ij})^2}$, obtained for the $P6_3cp$ structure of $LuFeO_3$ as the function of distance from the central Fe site. One can clearly see that the transfer integrals are limited mainly by the nearest neighbors (in the hexagonal plane), while the next-nearest neighbor transfer integrals are already considerably smaller, and all other parameters are negligible. This guarantees that the Wannier functions are well localized and our construction of the model Hamiltonian is very physical.

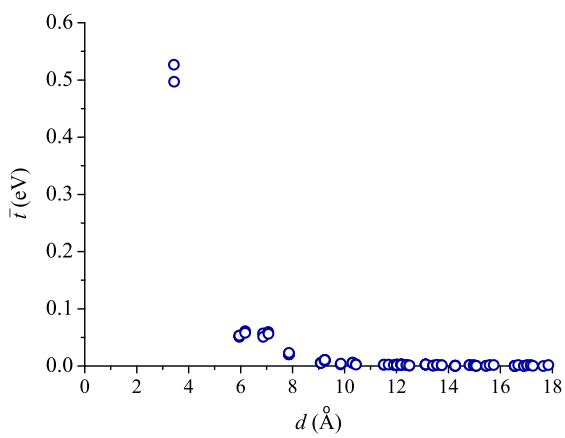

FIG. 1: (Color online) Distance-dependence of averaged transfer integrals $\bar{t}_{ij} = \sqrt{\sum_{ab}(t^{ab}_{ij})^2}$, obtained for the $P6_3cp$ structure of $LuFeO_3$. Two largest values at around $d \sim 3.4$ Å correspond to the nearest neighbors in the hexagonal plane. The next two group of values at around $d \sim 6$ and 7 Åcorrespond to the nearest neighbors between the planes and the next-nearest neighbors both in and between the planes.

Other examples can be found in the review article (Ref. 4) and in the previous publication

(Ref. 13).

II. DETAILS OF EXCHANGE INTERACTIONS CALCULATION BASED ON EXTENDED KUGEL-KHOMSKII MODEL

As shown in Fig. 1 of main text, the intra-layer superexchange (SE) interaction $H_{ex}^{a-b} = \sum_{i,j,Z_{Fe}} \mathcal{J}_{i,j}^{a-b} \vec{S}_i^{Z_{Fe}} \cdot \vec{S}_j^{Z_{Fe}}$ between two nearest neighbor (NN) Fe atoms at site i and j are mediated by corner sharing oxygen atoms. In order to elucidate the electronic structural origin, we employ the extended Kugel-Khomskii model and the SE coupling can be expressed as

$$\mathcal{J}_{i,j}^{a-b} = \sum_{\alpha,\alpha'} J_{\alpha,\alpha'}^{\mathrm{AFM}} + \sum_{\alpha,\beta} J_{\alpha,\beta}^{\mathrm{FM}} = \sum_{\alpha,\alpha'} \frac{4t_{\alpha\to\alpha'}^2}{\sum_{\alpha''} U_{\alpha'\alpha''} + \Delta_{\alpha\alpha'} + \sum_{\alpha''\neq\alpha}(J_{\alpha\alpha''}^{\mathrm{H}} - U_{\alpha\alpha''})} - \sum_{\alpha,\beta} \frac{4t_{\alpha\to\beta}^2 \sum_{\alpha''} J_{\beta\alpha''}^{\mathrm{H}}}{[\sum_{\alpha''} U_{\beta\alpha''} + \Delta_{\alpha\beta} + \sum_{\alpha''\neq\alpha}(J_{\alpha\alpha''}^{\mathrm{H}} - U_{\alpha\alpha''})][\sum_{\alpha''\neq\alpha}(J_{\alpha\alpha''-U_{\alpha\alpha''}}^{\mathrm{H}}) + \Delta_{\alpha\beta} - \sum_{\alpha''}(J_{\beta\alpha''}^{\mathrm{H}} - U_{\beta\alpha''})]} \quad (3)$$

In the above, $\alpha, \alpha', \alpha''$ run over all the half-filled d states and β runs over only the empty d levels. $t_{\alpha\to\alpha'}$ are NN hopping integrals between half-filled d states and $t_{\alpha\to\beta}$ describes the NN hopping integrals from half-filled to an empty d orbital. The hopping integrals are evaluated based on the localized Wannier functions.[7] generated from the energy window including ten $3d$ bands around the Fermi level of the DFT band structure. The matrix of Coulomb interactions of $3d$ bands are computed by applying the constrained DFT and the constrained random phase approximation.[8] considering the electronic screening. $J_{\alpha\beta}^{\mathrm{H}}$ is the intra-atomic Hund's coupling matrix, and $\Delta_{\alpha\alpha'(\beta)}$ is the crystal field splitting energies between α and α' or (β) states. The first term in Equ. (3) describes the AFM-type coupling resulting from virtual hopping processes between two half-filled d bands; while the second term depicts the competing FM-type coupling from hoppings from half-filled d orbital (α) to empty ones (β).

The matrices of screened Coulomb interactions $U_{\alpha,\alpha'(\beta')}$ based on localized Wannier functions and the intra-atomic Hund's coupling matrices $J_{\alpha\alpha'(\beta)}^{\mathrm{H}}$ for both hexagonal $LuFeO_3$ (hLFO) and hexagonal $LuMnO_3$ (hLMO) are presented in Table I, Table II, Table III, and Table IV respectively. One can easily see that the screened Coulomb interactions are at the same order of magnitude for both hLFO and hLMO.

According to the orbital symmetry on the hexagonal lattice sites, the hopping matrices have too independent super exchange paths Path_1 and Path_2 as shown in Fig. 2. In the

above, we have taken the $e'(x^2 - y^2, xy)$ as an example. In high symmetry structure with space group $P6_3/mmc$, the super exchange interactions in the two paths are equivalent. As a result, the two iron atom in both $path_1$ and $path_2$ have exact the same magnitude of exchange coupling energies. However, when the symmetry is lowed to $P6_3cm$ below the Curié temperature, $path_1$ and $path_2$ will break the symmetry and generate slightly different super exchange energies. In Table V, VI ,VII, VIII, we present the detailed information of the hopping matrices $t_{\alpha,\alpha'\beta}$ of both $path_1$ and $path_2$ in hLFO and hLMO. For simplicity, in the main text we only present the averaged super exchange coupling energies. The discussion of anisotropy in super exchange is beyond the scope of the current work.

The above calculations are based on the DFT ground state structure as shown in Table refStructures with space group $P6_3cm$. A plane wave cutoff of 500 eV is used with a $6 \times 6 \times \times 3$ k-point mesh centered at Gamma point. For transition metals, we choose $U = 4.5$eV and $J_H = 0.95$eV for hLFO and U=4,J=1 for hLMO.[9]. The criterion of residual Hellman-Feynman forces for geometry optimization is 0.001eV/Å.

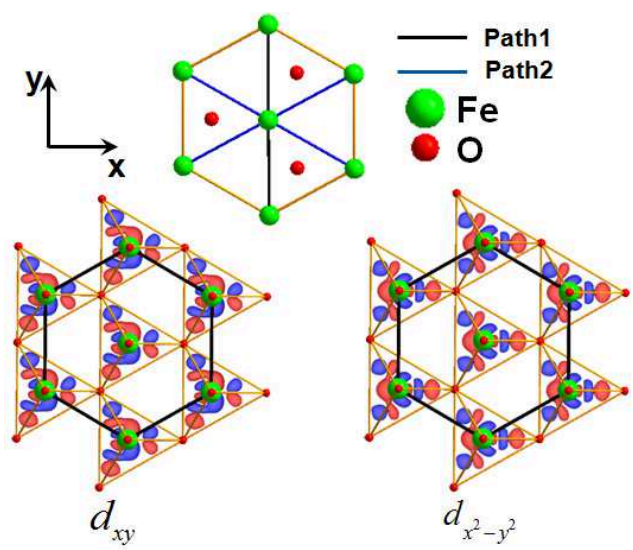

FIG. 2: Two nonequivalent in-plane exchange paths; Fe 3d d_{xy} orbits have the most contribution to path one and Fe 3d d_{x2-y2} have the most contribution to path two. (isovalue is chose to 0.02)

TABLE I: The matrices of screened Coulomb interactions $U_{\alpha,\alpha'(\beta)}$ (eV) based on localized Wannier functions in hLFO.

	d_{xy}	d_{yz}	d_{zx}	$d_{x^2-y^2}$	d_{z^2}
d_{xy}	3.494	2.193	2.192	2.686	1.859
d_{yz}	2.193	3.665	2.241	2.192	2.445
d_{zx}	2.192	2.241	3.666	2.192	2.445
$d_{x^2-y^2}$	2.686	2.192	2.192	3.492	1.859
d_{z^2}	1.859	2.445	2.445	1.859	3.214

TABLE II: The matrices of screened Coulomb interactions $U_{\alpha,\alpha'(\beta)}$ (eV) based on localized Wannier functions in hLMO.

	d_{xy}	d_{yz}	d_{zx}	$d_{x^2-y^2}$	d_{z^2}
d_{xy}	3.619	2.254	2.286	2.828	1.988
d_{yz}	2.254	3.580	2.261	2.253	2.500
d_{zx}	2.286	2.261	3.662	2.286	2.534
$d_{x^2-y^2}$	2.828	2.253	2.286	3.618	1.988
d_{z^2}	1.988	2.500	2.534	1.988	3.342

TABLE III: Intra-atomic Hund's coupling matrices $J^{\mathrm{H}}_{\alpha\alpha'(\beta)}$ (eV) in hLFO.

	d_{xy}	d_{yz}	d_{zx}	$d_{x^2-y^2}$	d_{z^2}
d_{xy}	0.000	0.699	0.699	0.403	0.754
d_{yz}	0.699	0.000	0.713	0.699	0.499
d_{zx}	0.699	0.713	0.000	0.699	0.499
$d_{x^2-y^2}$	0.403	0.699	0.699	0.000	0.753
d_{z^2}	0.754	0.499	0.499	0.753	0.000

TABLE IV: Intra-atomic Hund's coupling matrices $J^{\mathrm{H}}_{\alpha\alpha'(\beta)}$ (eV) in hLMO.

	d_{xy}	d_{yz}	d_{zx}	$d_{x^2-y^2}$	d_{z^2}
d_{xy}	0.000	0.676	0.676	0.395	0.738
d_{yz}	0.676	0.000	0.680	0.676	0.476
d_{zx}	0.676	0.680	0.000	0.675	0.476
$d_{x^2-y^2}$	0.395	0.676	0.675	0.000	0.738
d_{z^2}	0.738	0.476	0.476	0.738	0.000

TABLE V: Hopping matrix values $t_{\alpha,\alpha'(\beta)}$ (meV) of path$_1$ in hLFO.

	d_{xy}	d_{yz}	d_{zx}	$d_{x^2-y^2}$	d_{z^2}
d_{xy}	304.7	-69.0	-90.3	-100.4	-131.9
d_{yz}	69.0	-3.1	26.3	-9.6	-62.2
d_{zx}	-90.3	-26.3	-15.6	39.9	52.6
$d_{x^2-y^2}$	100.4	-9.6	-39.9	143.2	-88.4
d_{z^2}	131.9	-62.2	-52.6	-88.4	-137.4

TABLE VI: Hopping matrix values $t_{\alpha,\alpha'(\beta)}$ (meV) of path$_2$ in hLFO.

	d_{xy}	d_{yz}	d_{zx}	$d_{x^2-y^2}$	d_{z^2}
d_{xy}	199.3	-43.8	80.1	-167.4	158.8
d_{yz}	-24.6	-24.3	55.9	96.0	-71.7
d_{zx}	-33.0	-17.5	-0.1	1.3	-12.0
$d_{x^2-y^2}$	33.9	21.3	-93.7	282.1	-73.5
d_{z^2}	9.2	0.6	-86.9	177.8	-145.7

TABLE VII: Hopping matrix values $t_{\alpha,\alpha'(\beta)}$ (meV) of path$_1$ in hLMO.

	d_{xy}	d_{yz}	d_{zx}	$d_{x^2-y^2}$	d_{z^2}
d_{xy}	301.3	-81.3	-81.0	-130.8	-101.7
d_{yz}	81.3	-11.5	17.5	-8.3	-73.7
d_{zx}	-81.0	-17.5	-10.1	54.4	57.8
$d_{x^2-y^2}$	130.8	-8.3	-54.4	148.2	-89.0
d_{z^2}	101.7	-73.7	-57.8	-89.0	-196.4

TABLE VIII: Hopping matrix values $t_{\alpha,\alpha'(\beta)}$ (meV) of path$_2$ in hLMO.

	d_{xy}	d_{yz}	d_{zx}	$d_{x^2-y^2}$	d_{z^2}
d_{xy}	190.5	-51.6	76.4	-195.4	124.5
d_{yz}	-11.8	-15.3	49.8	86.4	-63.1
d_{zx}	-19.1	-22.4	2.3	-6.7	4.8
$d_{x^2-y^2}$	41.5	29.2	-71.5	276.3	-64.7
d_{z^2}	2.1	3.6	-64.6	134.0	-190.8

TABLE IX: Structure parameters of $P6_3cm$ hLMO and hLFO relaxed at DFT ground state.

			hLMO Exp.	hLMO Theo.	hLFO Exp.	hLFO Theo.
Lattice vectors		a($\AA$)	6.0268	6.0136	5.9652	5.9483
		c($\AA$)	11.3646	11.4149	11.7022	11.6943
Lu1	2a(0 0 z)	z	0.2788	0.2813	0.2721	0.2726
Lu2	4b(1/3 2/3 z)	z	0.2319	0.2343	0.2332	0.2276
Fe	6c(x 0 z)	x	0.3299	0.3334	0.3330	0.3340
		z	0.0000	0.0046	0.0000	-0.0039
O1	6c(x 0 z)	x	0.3012	0.3032	0.3030	0.3034
		z	0.1632	0.1694	0.1542	0.1614
O2	6c(x 0 z)	x	0.6409	0.6369	0.6490	0.6371
		z	0.3363	0.3403	0.3320	0.3323
O3	2a(0 0 z)	z	0.4774	0.4783	0.4720	0.4716
O4	4b(1/3 2/3 z)	z	0.0211	0.0274	0.0170	0.0170

III. TECHNICAL DETAILS OF DFT+U METHOD

In the calculations of spin phonon coupling, we perform DFT+U calculations using projector augmented-wave potentials with spin-orbit coupling using the spin-polarized generalized gradient approximation revised for solid (PBEsol) [15] as implemented in the Vienna Ab Initio Simulation Package (VASP) [14]. A plane wave cutoff of 500 eV is used with a $6\times6\times\times3$ k-point mesh centered at Gamma point. For transition metals, we choose $U = 4.5$eV and $J_H = 0.95$eV. The choice of effect U and J has been established in Ref. [16] based on the careful comparison of lattice constants, band gap between experiment and theory. The criterion of residual Hellman-Feynman forces for geometry optimization is 0.001eV/Å. We have adopted the four-state method[17] in computing the intralayer and interlayer exchange coupling constants, in which the total energies from DFT are used as inputs. In the DFT calculations of intra-layer exchange coupling, PBEsol is used without the on-site Coulomb U [13].

IV. EFFECTS OF SECOND NEIGHBOR IN SUPER SUPER EXCHANGE (SSE) AND PHONON COUPLINGS

In Fig. 3(a) of the main text, we have presented the ΔJ as functions of three phonon modes in hLFO, which are K_3, $K1$, and Γ_2^- respectively. In the main text, only Fe atoms in the first neighboring shell along the SSE paths are considered in the SSE energy fitting from density functional theory calculations. As a convergence check, in Fig. 3, we present the same dependences of ΔJ on the three phonon modes in which the both first and second nearest neighboring Fe atoms are considered. It can be seen that the K_1 mode persists to be the dominant role in tuning ΔJ, which confirm our main conclusion that the spin reorientation is driven mainly by K_1 phonon mode. This results also confirm our argument in the main text that the coupling between SSE and phonon modes are quantitatively converged and qualitatively accurate when first shell of neighboring Fe atoms are considered along the SSE paths.

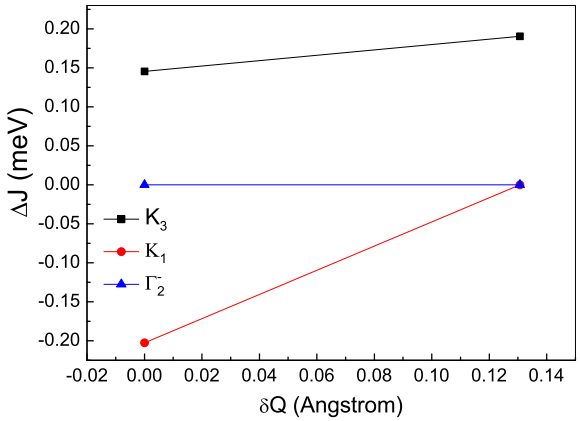

FIG. 3: (Color online) ΔJ as functions of increasing K_1, K_3, and Γ_2^- phonon modes individually frozen into the hLFO with P6$_3$/mmc symmetry, while the other two phonon modes are set to be zero. The reference point of each phonon mode is chosen to be the experimental mode amplitude at 300K [10]. In this case, the Fe atoms in both first and second neighboring shells are considered in the SSE energies fittings. Due to the largely increased computational time in choosing a larger supercell by including the Fe atoms in the second neighboring shell, we use sparser points of frozen mode amplitudes than those presented in Fig.3(a) of main text.

V. PHONON MODE DECOMPOSITION

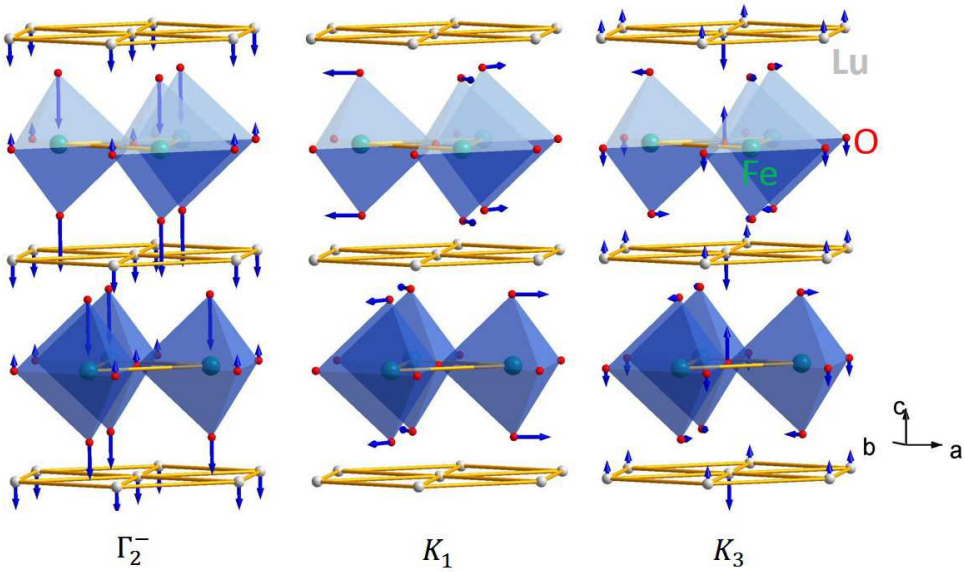

FIG. 4: (Color online) The illustration of the three phonon modes (Γ_2^-, K_1 and K_3) related to the P6$_3$/mmc to P6$_3$cm structural transition. We use the coordinate system of P6$_3$cm structure here (and throughout the paper) for the a, b and c axis. The rods connecting atoms are not to indicate chemical bonds, but to highlight the structural symmetry.

Table X displays the positions of the atomic sites of the P6$_3$cm structure and the corresponding P6$_3$/mmc structure. All the atomic positions are displayed using the P6$_3$cm coordinate system. For the P6$_3$cm structure, the experimental data at room temperature from Ref. [10] is used here. The P6$_3$/mmc structure is generated by moving the atomic sites of the P6$_3$cm structure to the symmetric position according to the P6$_3$/mmc symmetry; the only coordinates that can not be determined by the P6$_3$/mmc symmetry are the z-coordinates of the O$_{ap}$(1) and O$_{ap}$(2), as denoted by the variable z_{ap}.

To find the eigenvectors and displacements of the phonon modes, the following relations are needed

$$D_{i,\sigma} = \sum_p q_p \xi^p_{i,\sigma}/a_\sigma \tag{4}$$

$$\sum_{i,\sigma} n_i \xi^{p1}_{i,\sigma} \xi^{p2}_{i,\sigma} = \delta_{p1,p2}, \tag{5}$$

where $D_{i,\sigma}$ is the difference in coordinates of the atomic sites between the P6$_3$cm and

TABLE X: The atomic positions of the h-$LuFeO_3$ in $P6_3cm$ and $P6_3/mmc$ structures. The $D_{i,\sigma}$ is calculated from the difference between the atomic positions of the two structures, where i is the index of the atomic sites (e.g. Lu_1 and Fe), σ is the index of the displacement direction (e.g. [001] and [100]). The coordinate system of $P6_3cm$ is chosen for all the positions and displacements here. So the numbers are in the unit of the lattice constants of the $P6_3cm$ structure.

	$P6_3/mmc$	$P6_3cm$	$D_{i,\sigma}$	
			$\sigma = a$	$\sigma = c$
Lu_1	(0,0,$\frac{1}{4}$)	(0,0,0.2721)	0	0.0221
Lu_2	($\frac{1}{3}$,$\frac{2}{3}$,$\frac{1}{4}$)	($\frac{1}{3}$,$\frac{2}{3}$,0.2332)	0	-0.0168
Fe	($\frac{1}{3}$,0,0)	(0.333,0,0)	-0.0003	0
$O_{ap}(1)$	($\frac{1}{3}$,0,z_{ap})	(0.303,0,0.1542)	-0.0303	0.1542-z_{ap}
$O_{ap}(2)$	($\frac{2}{3}$,0,0.5-z_{ap})	(0.649,0,0.332)	0.0177 [a]	-0.168+z_{ap}
$O_{eq}(3)$	(0,0,$\frac{1}{2}$)	(0,0,0.472)	0	-0.028
$O_{eq}(4)$	($\frac{1}{3}$,$\frac{2}{3}$,0)	($\frac{1}{3}$,$\frac{2}{3}$,0.017)	0	0.017

[a]There is a sign reversal here because of the way that the representative $O_{ap}(2)$ is chosen.

$P6_3/mmc$ structure, q_p and $\xi^p_{i,\sigma}$ are the displacement and eigenvector of the phonon mode p respectively, a_σ is the length of the base a (lattice constant), and n_i is the number of atoms in atomic site i per unit cell. Eq. (4) provides the relation between the atomic positions, eigenvectors of the modes and the mode displacements; Eq. (5) comes from the

orthonormality of the eigenvectors. The symmetry of the Γ_2^-, K_1 and K_3 modes requires

$$\begin{aligned}
\xi_{i,a}^{\Gamma_2^-} &= 0 \\
\xi_{Lu_1,c}^{\Gamma_2^-} &= \xi_{Lu_2,c}^{\Gamma_2^-} \\
\xi_{O_{ap}(1),c}^{\Gamma_2^-} &= \xi_{O_{ap}(1),c}^{\Gamma_2^-} \\
\xi_{O_{eq}(3),c}^{\Gamma_2^-} &= \xi_{O_{eq}(4),c}^{\Gamma_2^-} \\
\xi_{i,c}^{K_1} &= 0 \\
\xi_{O_{ap}(1),c}^{K_1} &= \xi_{O_{ap}(2),c}^{K_1} \\
\xi_{O_{ap}(1),a}^{K_3} &= \xi_{O_{ap}(2),a}^{K_1} \\
\xi_{Lu_1,c}^{K_3} &= -2\xi_{Lu_2,c}^{K_3} \\
\xi_{O_{eq}(3),c}^{K_3} &= -2\xi_{O_{eq}(4),c}^{K_3}.
\end{aligned} \tag{6}$$

In addition, because the Γ_2^- mode has a zero wave vector, the center of the mass is not supposed to move. Thus, $\sum_{i,\sigma} \xi_{i,\sigma}^{\Gamma_2^-} n_i m_i = 0$, where m_i is the mass of the atoms at the site i.

TABLE XI: The decomposition of the distortion of the 300 K P6$_3$cm structure of h-LuFeO$_3$ from the P6$_3$/mmc structure in terms of the phonon modes Γ_2^-, K_1 and K_3. The $\xi_{i,\sigma}^p$ (dimensionless) in the table are the eigenvectors of phonon mode p. The variable z_{ap} is determined as 0.161.

	$\xi_{i,\sigma}^p$			
	Γ_2^-	K_1	K_3	
	$\sigma = c$	$\sigma = a$	$\sigma = a$	$\sigma = c$
Lu$_1$	-0.038	0	0	0.321
Lu$_2$	-0.038	0	0	-0.161
Fe	0.156	0.002	0	0
O$_{ap}$(1)	-0.193	0.289	-0.152	0
O$_{ap}$(2)	-0.193	0.289	0.152	0
O$_{eq}$(3)	0.257	0	0	-0.372
O$_{eq}$(4)	0.257	0	0	0.186
q_p (Å)	0.23	-0.13	0.94	

Combining Eq. (4-6), one can solve the mode eigenvectors $D_{i,\sigma}$, mode displacements q_p and the variable z_{ap}, as displayed in Table XI. The mode pattern of the Γ_2^-, K_1 and K_3

mode are illustrated in Fig. 4 according to the eigenvectors in Table XI. To point out several observations: 1) K_3 has the largest displacement, consistent with that of hexagonal manganites. 2) Unlike $YMnO_3$ or $LuMnO_3$, the displacement of the K_1 mode in h-$LuFeO_3$ is negative at room temperature, i.e. both Fe and O_{ap} move toward the nearest Lu along the [100] direction.

VI. ANALYSIS OF EXPERIMENTAL X-RAY ABSORPTION SPECTROSCOPY

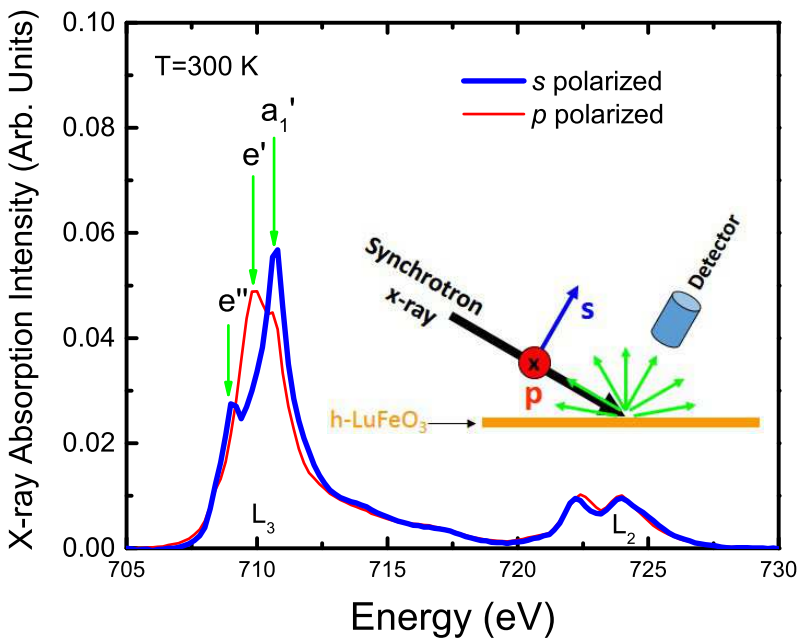

FIG. 5: X-ray absorption spectra of h-$LuFeO_3$ at 300 K, with the synchrotron x-ray in the s and p polarizations, as illustrated in the inset. The incident angle is 30 degree.

As shown in Fig. 5, x-ray absorption spectra show clear linear dichroism. In the a previous study [11], the peaks in the L_3 edge were attributed to the crystal field splitting levels using a symmetry analysis. In this study, temperature dependence of the x-ray absorption spectra were characterized. By fitting the peaks in the x-ray absorption spectra, we can trace the evolution of the crystal field levels with temperature.

Figure 6 shows the fit to the x-ray absorption spectra. By repeating the fit on spectra of different temperature, the temperature dependence of the crystal field levels can be found, as displayed in the Fig. 4(b) of the main text.

The two broad place-holding peaks are used here to account for features from other interactions (e.g. many-body interactions that may generate many satellite peaks causing broad features [18]) that may affect the shape of the x-ray absorption spectra. In principle the additional features in the fitting may introduce additional uncertainty. On the other hand, considering that the crystal field peaks are sharp and well-defined, this does not affect

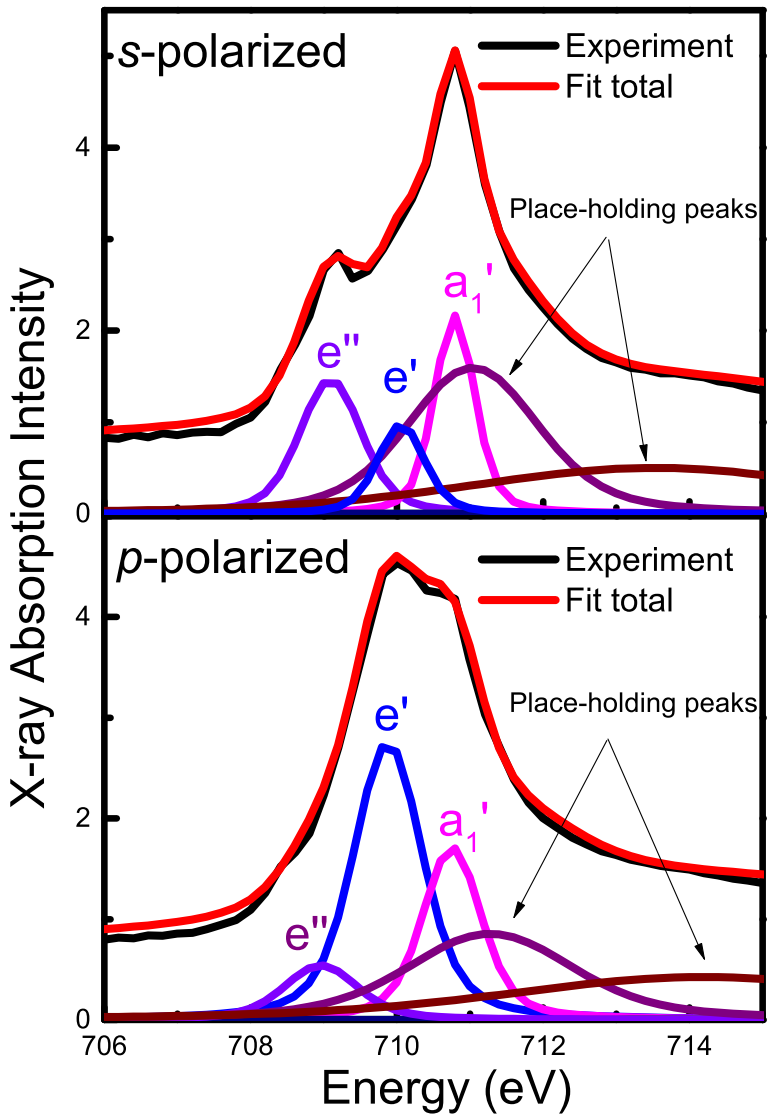

FIG. 6: Fit to the x-ray absorption spectra (200 K) for both s and p polarizations. Besides the three crystal field levels (e'', e', and a_1'), two place-holding peaks are included for the fitting.

our results significantly. As shown in Fig. 6, despite the significant difference between the two spectra (with s and p polarized x-ray), the peak positions of the crystal field levels are consistent.

A common trend (a broad, peak-like feature) is found in the temperature dependence of all the crystal field levels (see Fig. 4(b) of the main text). This feature is checked as the following: 1) By calculating the first moment of the spectra ($< E >= \frac{\sum E*I}{\sum I}$, where E is the energy and I is the intensity) near a certain crystal field peak, a similar trend is found, suggesting that the fit corresponds to the behavior of the spectra. 2) By repeating the fit on

both s and p polarized spectra, similar trends were found, which again suggests that the fit corresponds to the behavior of the spectra. 3) By calculating the temperature dependence of the x-ray dichroism, a similar trend is identified, suggesting that the trend can not be an artifact caused by a drift of the energy calibration.

VII. SIMULATION OF X-RAY ABSORPTION SPECTROSCOPY

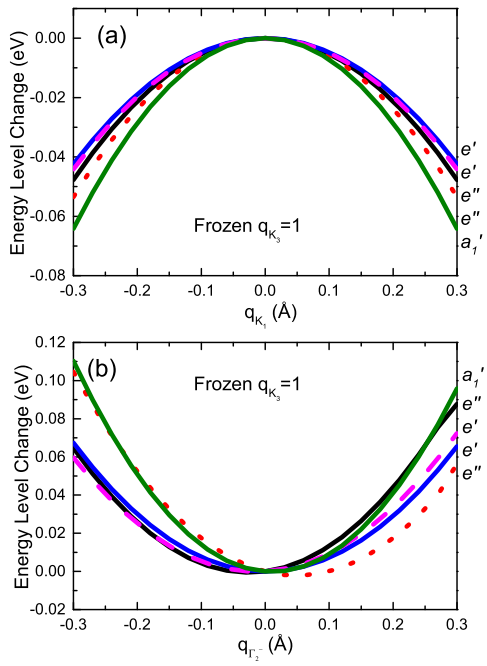

FIG. 7: Simulated crystal field energy levels as functions of the displacements of the K_1 (a) and Γ_2^- (b) phonon modes while the displacement of K_3 phone mode is set to 1 Å. The non-zero displacement of the K_1 (Γ_2^-) mode decreases (increases) the crystal field energy levels.

From the x-ray absorption experiments, we found that the Fe 3d crystal field levels move when the temperature is decreased. Since the crystal field levels are sensitive to the change of the local environment of the Fe, i.e. FeO_5 trigonal bipyramid, the phonon modes that distorts FeO_5 will affect the crystal field levels. Among the three phonon modes K_1, K_3 and Γ_2^-, K_3 mode represents a rotation of the FeO_5 along the [120] crystal axis passing Fe atom, relative to the rest of the lattice; this is expected to have a minimum impact on the crystal field levels because the displacement of the K_3 mode does not change the FeO_5 local environment as it changes slowly at low temperature (indicated by the XRD experiment). On the other hand, K_1 and Γ_2^- modes distort the FeO_5 local structure; they are expected to cause significant change of the crystal field levels.

The effect of the displacement of K_1 and Γ_2^- mode on the crystal field levels is simulated by representing the Fe 3d levels using the atomic orbitals in the hydrogen-like atoms. The crystal field levels are calculated by imposing the electrostatic potentials of point charges

from the oxygen anions in the FeO_5 structure. The eigenvectors in Table XI are used in the calculation. The displacement of the K_3 mode is fixed as $q_{K_3} = 1$ in the simulation.

Figure 7 displays the change of Fe 3d crystal levels as functions of the phonon mode displacements from the simulation. For Γ_2^- mode, the O_{eq} sites are moving away from the Fe; one O_{ap} site move rapidly toward the Fe site while the other O_{ap} site moves rapidly away. This pattern of shifting atomic sites causes the energies of all the crystal field levels to rise. Therefore, the displacement of the Γ_2^- mode alone cannot be a possible origin of the change of the crystal field level. For K_1 mode, since the O_{ap} sites move more than that of Fe site, the O_{ap} sites are effectively moving away from Fe when $|q_{K1}|$ increases, causing the lowering of all energy levels. Hence, there are two possible scenarios to explain the observed crystal field change in XAS experiments when the temperature is lowered: 1) q_{K_1} changes from a negative value to zero and to a positive value, resulting in a maximum of energy for all crystal field levels; 2) q_{K_1} and $q_{\Gamma_2^-}$ both change and the competition causes a peak in the measured Fe 3d crystal field levels.

[1] O. K. Andersen, Phys. Rev. B **12**, 3060 (1975); O. Gunnarsson, O. Jepsen, and O. K. Andersen, *ibid.* **27**, 7144 (1983); O. K. Andersen, Z. Pawlowska, and O. Jepsen, *ibid.* **34**, 5253 (1986).

[2] N. Marzari N and D. Vanderbilt, Phys. Rev. B **56**, 12847 (1997).

[3] I. V. Solovyev, Z. V. Pchelkina, and V. I. Anisimov, Phys. Rev. B **75**, 045110 (2007)

[4] I. V. Solovyev, J. Phys.: Condens. Matter **20**, 293201 (2008).

[5] F. Aryasetiawan, M. Imada, A. Georges, G. Kotliar, S Biermann, and A. I. Lichtenstein, Phys. Rev. B **70**, 195104 (2004).

[6] L. Vaugier, H. Jiang, and S. Biermann, Phys. Rev. B **86**, 165105 (2012).

[7] I. Souza, N. Marzari N and D. Vanderbilt, Phys. Rev. B **65**, 035109 (2001); N. Marzari, A. A. Mostofi, and D. Vanderbilt,Rev. Mod. Phys. **84**, 1419 (2012);

[8] B. C. Shih, Y. Zhang, W. Zhang, and P. Zhang, Phys. Rev. B **85**, 045132 (2012); T. Miyake and F. Aryasetiawan, Phys. Rev. B **77**, 085122 (2008);

[9] Das, H. et al. Bulk magnetoelectricity in the hexagonal manganites and ferrites. Nat. Commun. 5:2998 doi: 10.1038/ncomms3998 (2014). J. Hong, A. Stroppa, S. Picozzi, and D. Vanderbilt, Phys. Rev. B **85**, 054417 (2012);

[10] E. Magome, C. Moriyoshi, Y. Kuroiwa, A. Masuno, and H. Inoue, Japanese Journal of Applied Physics **49**, 09ME06 (2010).

[11] Wang, W, *et al.* Crystal field splitting and optical bandgap of hexagonal $LuFeO_3$ films. *Appl. Phys. Lett.* **101**,241907 (2012).

[12] S. Lee, A. Pirogov, and Misun Kang.et al, Nature **451**, 805-808 (2008);

[13] I. V. Solovyev, M. V. Valentyuk, and V. V. Mazurenko,Phys. Rev. B **86**, 054407 (2012).

[14] G. Kresse, and J. Furthmüler, Phys. Rev. B, **54**, 11169 (1996).

[15] J. P. Perdew, *et al*, Phys. Rev. Lett. **100**, 136406 (2008).

[16] H. Das, *et al.*, Nat. Commun., in press.

[17] H. J. Xiang, E. J. Kan, S. Wei, M.-H. Whangbo, and X. G. Gong, Phys. Rev. B **84**, 224429 (2011).

[18] J. Stohr, H.C. & Siegmann. Magnetism from fundamentals to nanoscale dynamics. Berlin: Springer (2006)